**Solid Freeform Fabrication 2019: Proceedings of the 30th Annual International**
**Solid Freeform Fabrication Symposium – An Additive Manufacturing Conference**
**Reviewed Paper**

# Localized Effect of Overhangs on Heat Transfer during Laser Powder Bed Fusion Additive Manufacturing

Basil J. Paudel[1], Scott M. Thompson[2]

[1]*Department of Mechanical Engineering, Auburn University, Auburn, AL 36849*

[2]*Department of Mechanical & Nuclear Engineering, Kansas State University, Manhattan, KS 66506*

*Corresponding author: smthompson@ksu.edu

## Abstract

The current study concentrates on the effect of local part topology on heat transfer during the laser-powder bed fusion (L-PBF) additive manufacturing (AM) process. The high heat flux diffusion (i.e. thermal spreading) is numerically modeled and investigated for the L-PBF of a thin-walled part with various negative draft angles (overhangs) and a thin wall of variable cross-sectional area. Scan-wise and layer-wise manufacturing effects on heat transfer are quantified via peak melt pool temperature and resulting melt pool morphology. These thermal metrics are used to understand the effect of overhang angles on the melt pool mand the surface roughness traits of stainless steel 316L, Inconel 625 and Ti-6Al-4V parts. Both powder effects and phase change within the melt pool are considered using approximate, reduced-complexity techniques. The employed numerical model has been validated using data available in the literature. Results demonstrate that the melt pool morphology and temperature distribution along build geometries with negative draft angles are significantly different than those with positive draft angles.

**KEYWORDS:** Laser-Powder Bed Fusion, Heat transfer, Simulation, Multi-pass, Numerical methods

## Introduction

Laser-based powder bed fusion (L-PBF) utilizes a powder bed platform that can change height in increments of micrometers to accomplish layer-by-layer additive manufacturing (AM). Initially, a coater distributes the metal powder across the build platform. Intense laser irradiation is concentrated at a micron-sized spot in order to provide sufficient energy to melt the powder. As the laser moves with a speed on-the-order of ~1 m/s per instructions from computerized numerical control, the melt pool quickly solidifies and creates a track of solid metal which is repeated over numerous patterned tracks to form a complete layer. To form a complete 3-dimensional part, the build platform then lowers by the specified layer thickness. This process is re-iterated for several slices of the input design resulting in a part with near net shape and relatively fine quality. More recently, AM technologies such as L-PBF have gained traction in industry for engineering material with unique specifications while minimizing supply chain costs. Employing AM technology provides benefits from the consolidation of multiple phases in material production into a simple process. Another advantage of L-PBF comes from the re-usability of the un-used powder resulting from the un-sintered powder bed. While the benefits for AM surmount, this relatively new technology still has complications that arise, mainly due to the fast-moving, small-sized laser heat source.

Engineering a customized part requires knowledge of a material's thermal history from the melting to solidification phases. With the proper physical modeling, one can determine the temperature distribution and gradients within the part for estimating the evolution of the material structure during AM. While this is easier said than done, challenges await in the ability of predicting the thermal history and cooling rates due to opposing scales associated with the heat source size and velocity, respectively. Analytical solutions for the melt pool and heat affected zone (HAZ) temperature distributions have been developed, or in some cases modified, from the solutions pertaining to welding applications. The earliest solution dates to Rosenthal [1] for the moving point heat source on a semi-infinite solid. However, Rosenthal's model and its predecessors are generally limited to standard geometries with very simple shapes. To ease computations for various practicing engineers, researchers have developed 'process maps' [2–4]. These maps provide a 2D/3D visualization of analytical models – providing relationships between temperature, mechanical properties and process parameters for assisting the AM process design. More recently, there has been an overwhelming amount of numerical studies performed to better understand the multi-physical processes involved during L-PBF [5–10].

In general, the quality of any fabricated, metallic part depends on the process parameters used in the manufacturing process. For L-PBF, the major process parameters that affect part quality are laser power, scan speed, hatch spacing, layer thickness, build orientation, and part position within the platform [11]. Dimensional or non-dimensional groupings of parameters such as the volumetric energy density (VED), *Peclet*, *Marangoni*, *Biot*, and *Fourier* numbers can be used for process mapping for predicting process-property relationships more agnostically. For example, a low energy density may result in low quality parts due to the presence of lack of fusion (consequence of insufficient energy to melt powder) and/or voids, while high density increases warping and spatter generation [12].

Many research studies have concentrated on predicting the melt pool shape and size during a single layer L-PBF process simulation. Multi-pass laser simulation studies have found very little traction in research due to computational time required to perform such multi-physical approaches. In general, multiphysics approaches involving powder, liquid melt pool or laser-powder-melt pool interactions have been limited to single track simulations [9,13–16].

One of the most overlooked process parameters in L-PBF is the build orientation. Multiple studies [17–19] reported the inability of L-PBF, also AM in general, to produce consistent microstructure in the part. Yadollahi et al. [19] studied the fatigue performance of additively manufactured stainless steel 17-4 PH in different build orientations, and attributed the drop in the performance to the direction of the un-melted plane between layers with respect to the loading direction. While those results show some evidence to the difference in performance, Hartunian and Eshraghi showed inherent differences on the microstructure resulting due to orientation of heat dissipating direction. Their study also pointed that the horizontally-built samples close to the substrate presented brittle fracture features while the ones away showed ductile fracture features. Simonelli et al. [20] studied the microstructure and fatigue performance of L-PBF Ti-6Al-4V, however, they reported that for the specimens tested, no difference exists between specimens at varying distances from the substrate. They also observed predominant columnar grains in the fabricated part, and attributed it to the track-wise and layer-wise nature of the AM process.

Fox et al. [21] studied the effects of surface angle (with respect to the horizontal build plane) on the surface roughness of L-PBF parts. The study showed that surface roughness (*Ra*) increases with increasing overhang angles. While these results are consistent with what has generally been reported in the literature, these authors concluded that a definite correlation between surface angle and the *Ra* does not exist.

Build orientation has been very often used as a design parameter for manufacturing, and is found to affect the final material properties as well as part-performance. For example, specimens built at 45 °C to the horizontal plane were found to have greater surface roughness and resulting in earlier fatigue failure. However, in a microscale, any layer fabricated on top of a powder particles instead of solid clad can be treated as an overhang. A schematic of a localized overhang region anticipated in layer-wise manufacturing process due to varying cross section area is shown in Figure 1. While numerous studies have shown performance differences due to build orientation, the thermal phenomena/characteristics within impactful regions have rarely been characterized. This current study focuses on the effects of negative draft angles and part overhangs, characterized by an overhang angle, on the peak temperature, bulk/sensible heating and t melt pool shape along a part. The study focuses on the L-PBF of Ti-6Al-4V, stainless steel 316L, and Inconel 625 (IN625) - which are all typical materials used for metals AM.

## Problem setup

Numerical studies were conducted for three materials commonly used in the AM industry: Ti-6Al-4V, IN625, and stainless steel 316L. All numerical simulations were performed using the commercial software package, Comsol Multiphysics 5.4, on the Hopper supercomputing cluster at Auburn University. The thermophysical properties for each material were taken from the open literature [22–24]. Initially, single pass simulations ware tested for IN625, and results validated against the experimental data from Ref. [25]. Numerically-predicted and experimentally-measured melt pool dimensions are tabulated in Table 1 for two different laser scan speeds. For both validation studies a nominal laser power of 195 W was used. The scan speed was set at 800 mm/s for Case A, and 500 mm/s for Case B. The laser was modelled using a Gaussian beam intensity that decays exponentially with distance from the center. The numerically-predicted melt pool dimensions were found to agree within 10% of the experimental values for both cases as shown in Table 1. Discrepancies between numerical and experimental values is partially attributed to the uncertainty in absorptivity (0.35 is currently used) and material properties for the liquid state. The numerical study consistently overpredicted the melt pool dimensions for both cases. However, since the current study only concentrates on the qualitative trends results from relatively slight process parameter variation, no further adjustment was deemed necessary. Mesh independence studies were performed and no significant changes in melt pool dimensions were found. The mesh used for multi-pass simulations is shown in Figure 2. Due to adaptive time stepping, no time independence study was required.

Table 1: Comparison of melt pool dimensions between simulation and experimental data for single pass study

| | | **Experimental (µm)** | **Numerical (µm)** | **% Error** |
|---|---|---|---|---|
| *Case A 800 mm/s* | Melt pool width | 133.0 | 134.3 | 1.0 % |
| | Melt pool depth | 38.0 | 40.8 | 7.4 % |
| | Width/depth ratio | 3.5 | 3.3 | 6.0 % |
| *Case B 500 mm/s* | Melt pool width | 162.0 | 154.8 | 4.4 % |
| | Melt pool depth | 49.0 | 50.0 | 2.0 % |
| | Width/depth ratio | 3.3 | 3.1 | 6.1 % |

The current study accounts for powder presence at a continuum scale using a modified thermal conductivity value. The powder bed thermal conductivity was taken as ~1-2% of the solid value based on relations proposed in the literature [26–28]. Through the usage of the ‘Irreversible Transformation’ feature provided by the software module, which keeps track of the material form, the current study accounts for powder to melt pool transformation (irreversible) and liquid to solid form through phase change phenomenon. This combination allows for a more convenient phase tracking in the module. The powder to melt pool (irreversible) transformation was designed to occur when the local powder temperature exceeded the liquidus temperature for at least a tenth of a millisecond (100 µs). The time step was determined based on the characteristic melting time for a mean powder size of 20 µm via the relation $t = L^2/\alpha$ as a first approximation. Both radiation and convection heat transfer losses along the top surface of the powder bed, as well as the exposed solid surfaces, were accounted for. A convection coefficient of 15 W/m$^2$K was used to model forced convection within the build chamber and is within the range of values reported in the literature [16,29]. For all cases, the substrate temperature was set to 20 °C except for the initial validation study where the model followed similar boundary conditions as the reported experiment. Powder absorptivity values were taken from Ref. [30] for IN625 (0.65), SS 316L (0.65) and Ti-6Al-4V (0.71), and are usually reported to be ~2-7 times higher than the flat surface absorptivity due to powder shape, surface roughness and oxidation.

The peak melt pool temperature was found to be steady within a fraction of a millisecond. As such, the transient study was conducted for an L-PBF track length 10 times the beam radius to save computational time. The clad was then allowed to cool off for a duration equal to 25 times the beam radius during which the average clad temperature cools down to a tenth of melting point temperature. Other simulation parameters are listed in Table 2. For the subsequent layer, the laser scans from the first overhang along the clad beneath and ending at the second overhang.

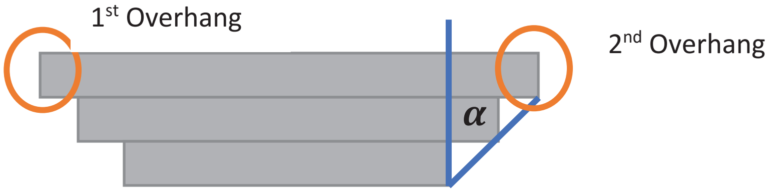

Figure 1: Schematic showing 1st and 2nd overhangs in subsequent layer scans during fabrication of a single-track, thin wall with negative draft angle

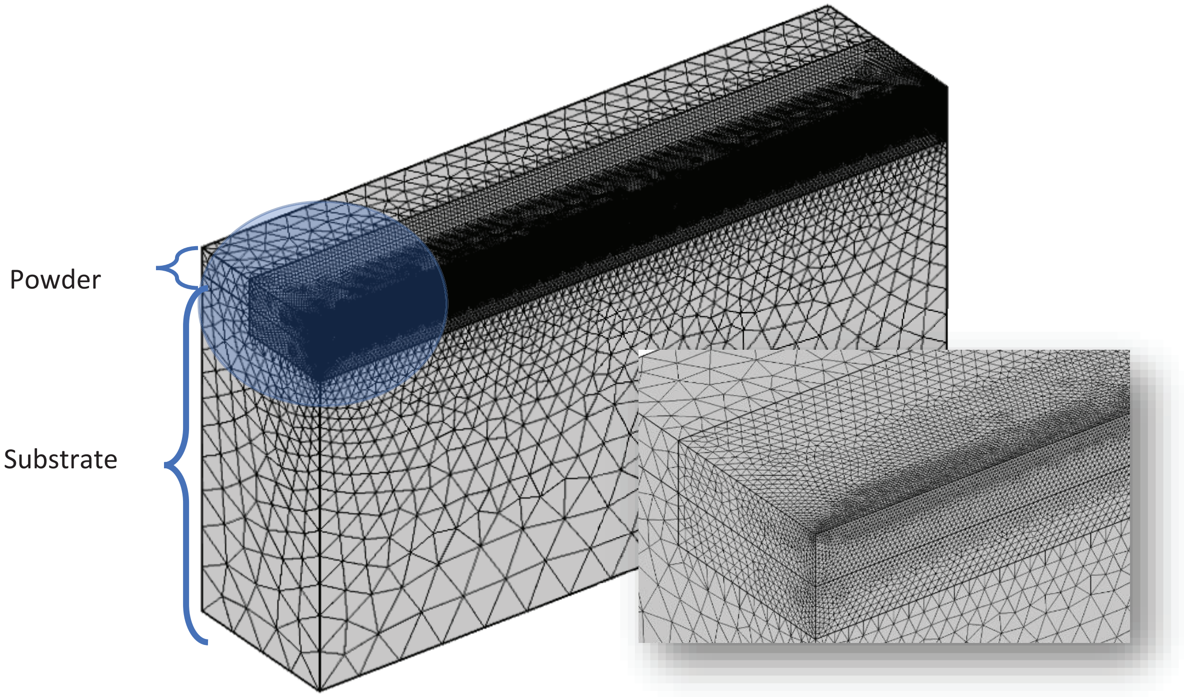

Figure 2: Mesh used for multi-pass study at an overhang region

Table 2: Simulation Parameters

| Materials | Ti-6Al-4V | IN625 | 316L |
|---|---|---|---|
| Substrate temperature | 20 °C | | |
| Laser power | 100 W | | |
| Scan speed | 500 mm/s | | |
| Beam diameter | 140 µm | | |
| Layer thickness | 40 µm | | |
| Hatch spacing (for multi-pass) | 0.1 mm | | |
| Track length | 0.7 mm | | |
| Time between successive passes | 25 × (track time) | | |

## Results and discussion

### Multi-pass effects

This current multi-pass L-PBF study shows that the melt pool dimensions increase significantly between the first pass and the subsequent passes within the same layer and has the potential to stabilize over time. The stabilization in melt pool size tends to be associated with longer tracks. Shorter tracks, for example, when checkerboard scan patterns are being used or when the track length available is small due to part thickness in the direction of laser scan, may not allow for such stabilization, and this can leave the entire layer with non-uniform melt pool dimensions, as has been observed in the published studies.

The ability to predict the melt pool shape along with the cooling rate and thermal gradient is particularly important in understanding grain evolution within a part. Most studies that rely on single-track L-PBF simulations show symmetric melt pool shapes. However, in practice this may only exist for the first few tracks of a layer partition/island. With multiple passes, the already solidified clad on one side and the powder on the other side of the track, conduction heat transfer occurs unevenly, mostly on the side of the already solidified track. Only a fraction of heat dissipates through any local powder. As a result, the instantaneous melt pool shape is highly asymmetrical, as shown in Figure 3. Additionally, in the depth-wise direction the melt pool shape becomes flatter due to the presence of powder bed on the side. The ability to predict the melt pool shape along with the cooling rate and thermal gradient is particularly important in understanding and predicting material grain evolution.

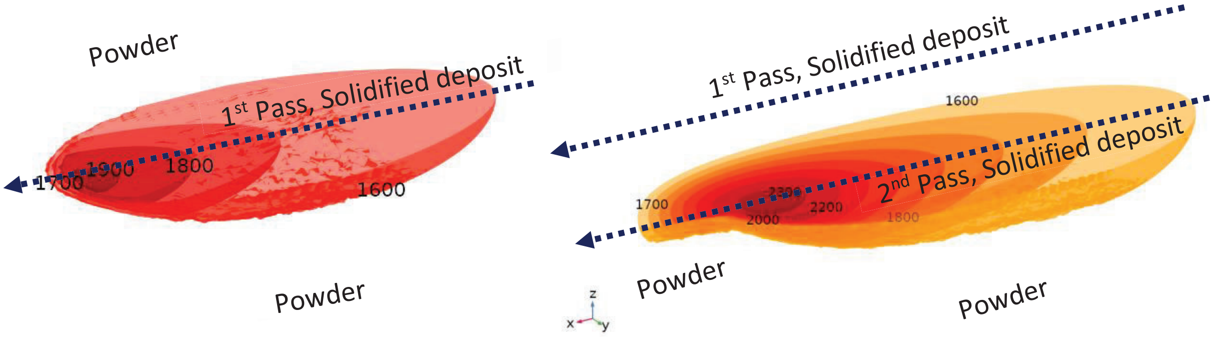
Powder
1st Pass, Solidified deposit
1700
1900
1800
1600
Powder
1st Pass, Solidified deposit
1600
1700
2300
2200
2000
1800
2nd Pass, Solidified deposit
Powder
Powder
z
x
y

Figure 3: Simulated melt pool shape isothermal contours (in ºC) resulting from single track vs. multi-track laser scan in IN625 (arrows show path of laser beam center and scan direction)

### Multi-layer scanning and overhang effects

The melt pool when the powder material sits beneath the layer under processing has also been investigated herein. This scenario occurs during the L-PBF of a part with overhangs; with overhang orientation quantifiable via an overhang (or draft) angle. The thermal phenomenon during L-PBF of the overhang is quite unique in the sense that energy dissipation occurs through a limited interfacial surface area. This results in a more constrictive heat flow through the melt pool which is in contrast to the thermal spreading that occurs on builds with positive draft angles. There is a high thermal resistance associated with the low thermal conductivity of the powder surrounding the melt pool in the overhang region.

The melt pool dimensions for the first pass and second pass (at the start of the laser scan) for an overhang angle of 60° are shown in Figure 4. The results from the single track, multi-layer study, with a scan speed of 500 mm/s and an absorbed power of 60 W, show that the melt pool width does not change significantly between subsequent laser passes. However, melt pool depth increases considerably at the overhang region between the first pass and the second pass. A second case study on IN625 was performed with increased scan speed of 800 mm/s and higher absorbed power of 120 W. Results for this scenario (not shown) show that both the melt pool width and depth have similar trend – unlike what was observed for the previous case with 500 mm/s and 60 W, and worthy of further investigation but not included in this study.

The melt pool depth was found to not increase as much after the third pass during L-PBF. It was found that there is a slight pull down on the melt pool depth dimension around 40 μm which corresponds to the powder layer thickness. The slight resistance towards deepening the melt pool is due to the powder-transformed-melt-pool meeting the cooler solid substrate/deposit which is capable of higher heat transfer rates. Likewise, the overshooting of the melt pool depth can be explained by the fact that at the overhang region, the laser thermal energy only penetrates 72 μm through the powder due to its substantially low thermal conductivity. As soon as the laser beam scans the region with solid mass beneath the powder layer (non-overhang region), the melt pool depth sinks suddenly due to the higher heat transfer rate provided by the solid clad. This sudden quenching of this melt pool in the overhang region may consequently affect the material properties resulting in a more brittle partial region/surface within the fabricated part. These changes in the melt pool geometry can be considered solely due to the overhang effects. This shows that the L-PBF of overhang structures is a highly localized process isolated from the effects of substrate temperature or bulk heat accumulation in the cladded region. At the non-overhang region, the melt pool dimension (width and depth) increases slightly with subsequent layers due to bulk heat accumulation.

It was found that the melt pool morphology at an overhang at the end of the track differs from the first overhang leading to different temperature distributions within the melt pool and HAZ. Melt pool formation at the beginning of the track consists of first superheating newly deposited powder initially at room temperature to melting temperature in order to fuse with the previous layer. In contrast, during the formation of the clad at the end-of-track overhang (2nd) region, a fused melt pool already exists on the tail region of the newly formed overhang. Since the tail is already above melting temperature of the powder, absorbed laser energy enables more powder to melt in the overhang region. This allows for the end-of-track melt pool to grow even larger than the one at the beginning of the track (1st overhang).

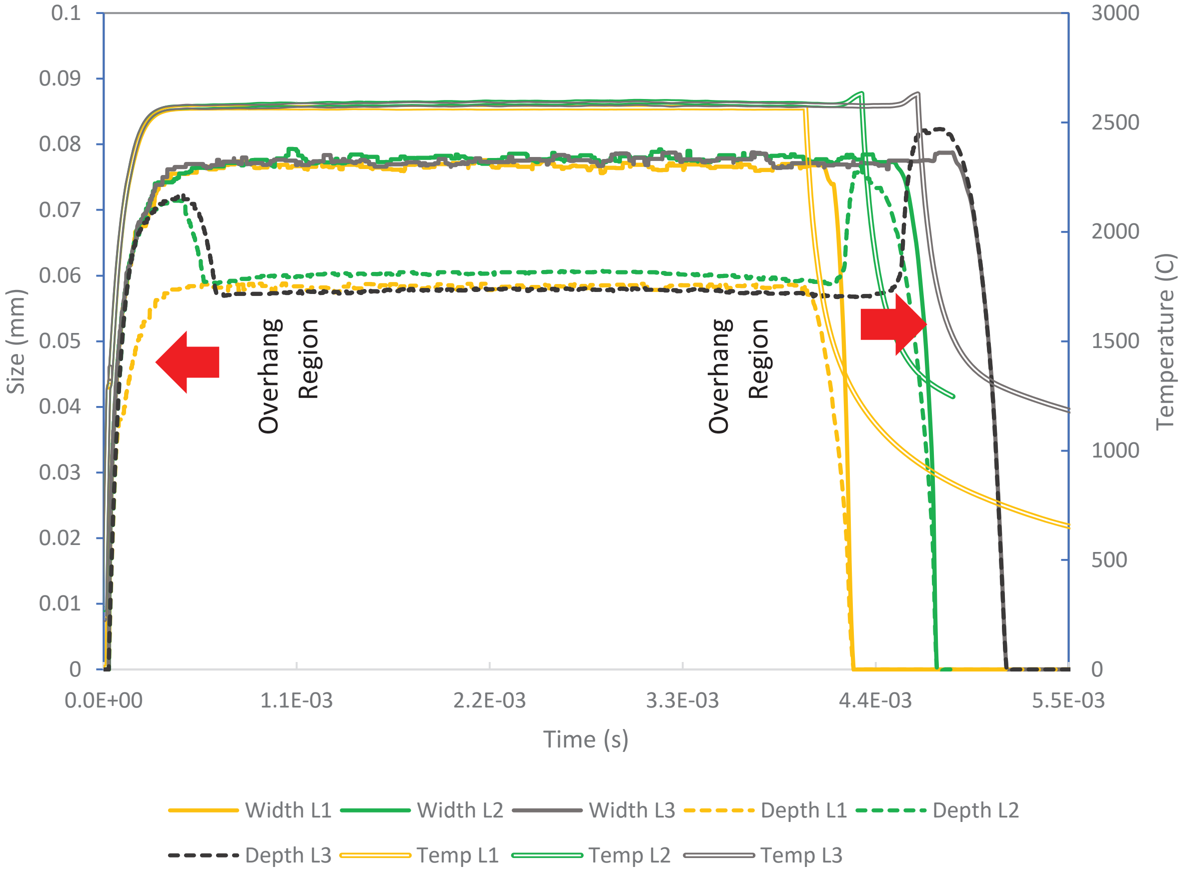

Figure 4: Melt pool dimensions and maximum temperature for the first (L1), second (L2) and third (L3) laser pass for Inconel 625 at 500 mm/s scan velocity and 60° negative draft angle

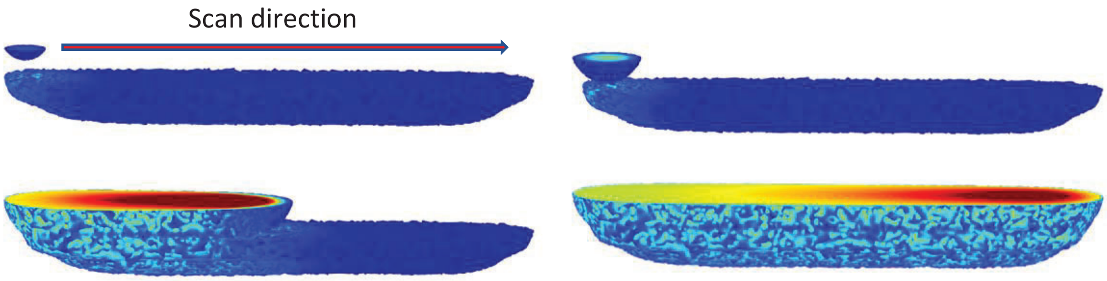

Figure 5: L-PBF of a clad along the second layer for overhang of 30° in IN625 at different time steps of melt pool formation; top-left shows melt pool nucleation on top of powder, top-right shows melt pool fusion with previous layer, bottom-left shows progressive melt pool, bottom-right shows final melt pool

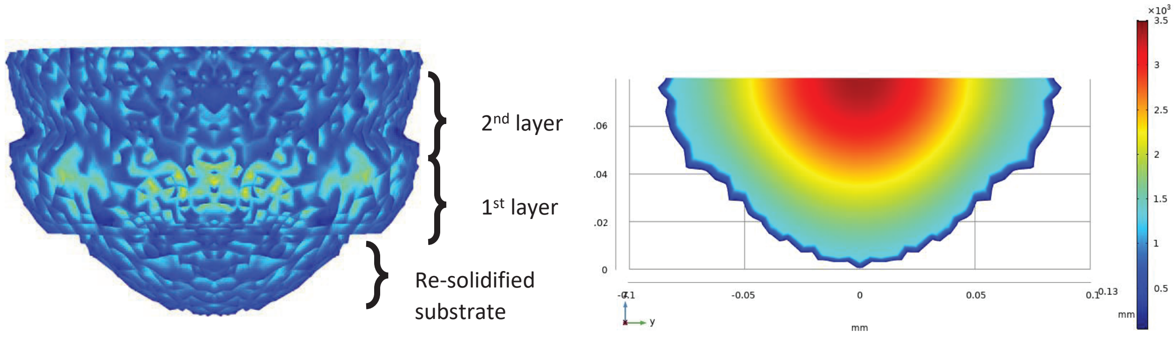

Figure 6: Multi-layer single track bead view (left) of melt pool showing re-solidified substrate, first layer and second layer of deposit (unmelted powder and substrate not shown); and melt pool temperature profile (right) halfway during second layer scan

Figure *5* shows the melt pool during the L-PBF of a new IN625 layer on top of an existing solidified layer with a 30° overhang angle for a track length of 0.7 mm. It may be seen that, during the first few microseconds, a disconnected melt pool is formed which grows and ultimately fuses with the previously formed clad. The maximum melt pool temperature during the laser scan along the part/powder does not change considerably in subsequent passes. This is because of inter-layer dwell time after each layer scan and the addition of fresh powder at room temperature. Similarly, due to low powder conductivity and the time scale associated with the process, the top surface of the powder bed can be considered thermally isolated from the deposited clad. Consequently, maximum thermal energy is stored at the top surface of powder bed.

The width-wise direction of the melt pool, as shown in

Figure 6, shows more irregularity with respect to each successive layer. Although this does not immediately affect the undersurface of the overhang, this effect is present in most layer-wise additive processes even for parts built vertically-upward with zero draft angle. This effect is more pronounced when the layer thickness approaches the maximum melt pool dimensions for the selected powder material and process parameter combination. Conversely, when the power is high enough giving rise to higher melt pool dimensions, this quenching effect may not be as visible due to earlier contact with the solid deposit. The effect of power and velocity will be a task for future study.

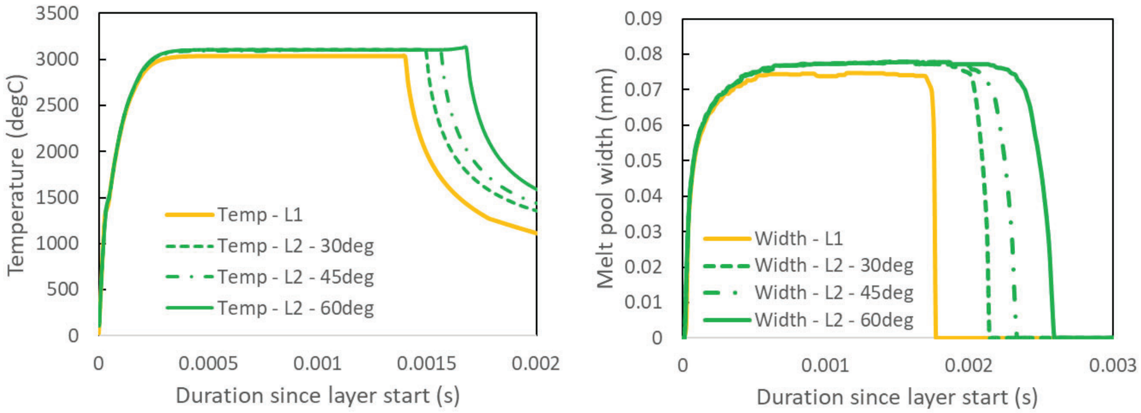

Figure 7: Comparison of peak melt pool temperature (left) and width (right) between first layer (L1) and second layer (L2) for different overhang angles on stainless steel 316L; L1, L2 in the legend refers to data from layer 1 and layer 2 respectively.

The peak melt pool temperature during the first and second laser scan for stainless steel 316L at various overhang angles is plotted in Figure 7. It may be seen that no significant change in maximum temperature occurs within the overhang region as compared to the non-overhang despite the difference in angles. For an overhang angle of 60º and for stainless steel 316L, the increase in maximum melt pool temperature is 0.6% of the value at the non-overhang region for first overhang layer, whereas it increased to 1% at the second overhang. For lower draft angles, the increase in temperatures were less than 10 °C (<0.1%), and within the numerical margin of error. Similarly, the melt pool width did not seem to be affected solely by the overhang angle for the parameters tested against. In general, the results demonstrate that, for chosen laser scan speed, power and material, no significant difference in peak melt pool temperature exists at the overhang although a slight increase in temperature occurs in successive layers due to bulk heat accumulation as shown in Figure 7.

For a given material the melt pool depth was found to be affected by the degree of overhang (overhang angle). The evolution of melt pool depth at different layers, overhang angles and powder material are tabulated in Table 3. Results indicate that no significant variations were realized at 30° overhang angles, although the melt pool temperature distribution at the end-of-track overhang has a slight spike in the value. By a 45° overhang angle, the both start-of-track and end-of-track overhangs showed increase in melt pool depth. The melt pool at the start-of-track overhang was found to be smaller than the one formed at the end of the track. This can be attributed to the initial thermal transiency within the melt pool and direction of laser scan. A deeper melt pool seems to be formed for a longer amount of time at the end-of-track overhang region. With increases in the overhang angle, the difference in the melt pool depth appears to narrow between the two overhangs each lasting for comparable amount of time.

For a relatively low overhang angle of 30°, low surface roughness is predicted by the model in the overhang surface. Note that due to the single-track but multi-layer nature of the current study, thickness of overhang surface is equal to the melt pool width dimension. Deeper melt pools in the overhang region affect the expected dimensional accuracy of the fabricated part. Regions with overhang structures may fall out of tolerance due to increased melt pool depth. While it is commonly understood that dimensional inaccuracy of L-PBF parts with overhangs has been due to the lack of support underneath, the results herein provide additional reasoning based on the local heat transfer within the overhang region.

Results also indicate that at higher overhang angles, the melt pool depth increases in the vicinity of the overhang. This is due to the high thermal resistance of the surrounding powder bed at the overhang region. Similarly, a comparison of the melt pool depth, as shown in Table 4, between the first overhang (on 2nd layer) and the overhang on the 3rd layer, shows a significant increase in melt pool depth. This is attributed to the fact that during the L-PBF of the second overhang (third layer), the melt pool is formed next to the previous overhang. As a result, the subsequent melt pool (second overhang) heat transfer experiences higher thermal resistance from the solid overhang as compared to the melt pool formed in the earlier layer. Unlike the other two materials, Ti-6Al-4V does not show significant change in the melt pool dimension in the first overhang.  This may be the result of high melting point temperature and the absorbed power combination. Surprisingly, the absorbed energy overwhelms the material in the subsequent overhang resulting in the similar increase in the melt pool depth.

Table 3: Comparison of melt pool depth at different layers and negative draft angles on various powder bed materials

| Ti-6Al-4V | IN625 | SS 316L | |
|---|---|---|---|
| 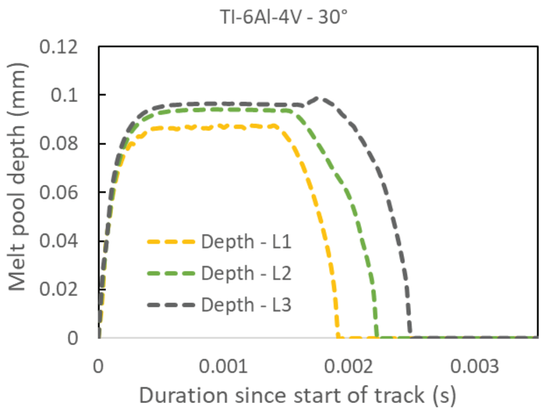 | 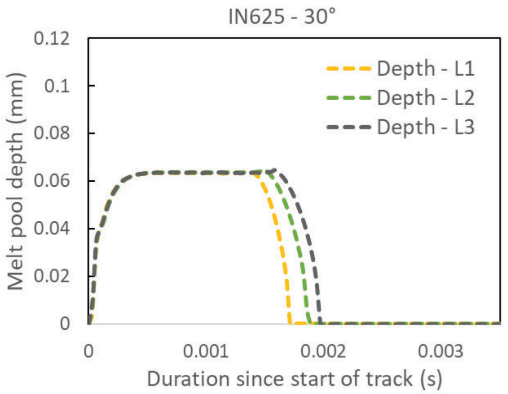 | 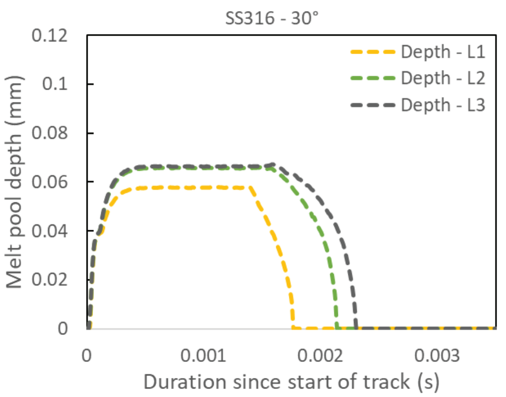 | 30 ° |
| 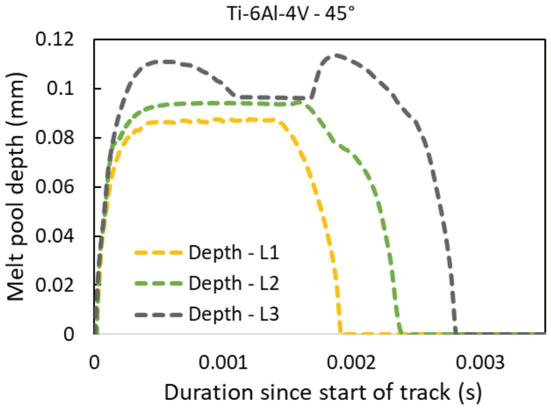 | 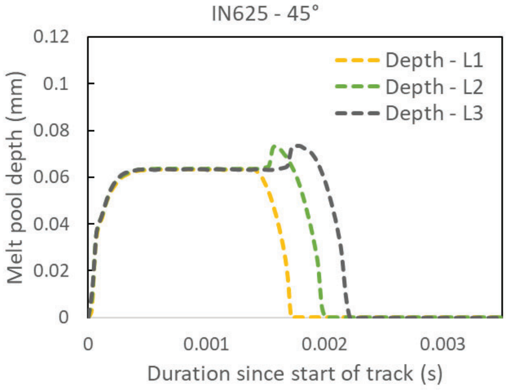 | 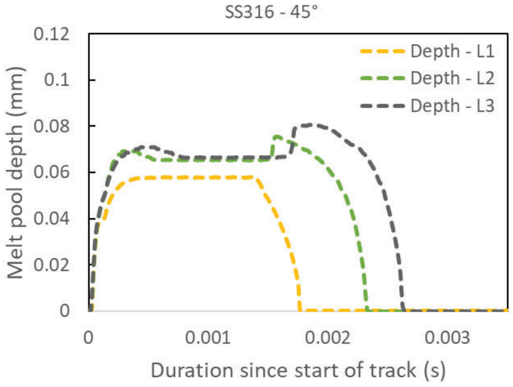 | 45 ° |
| 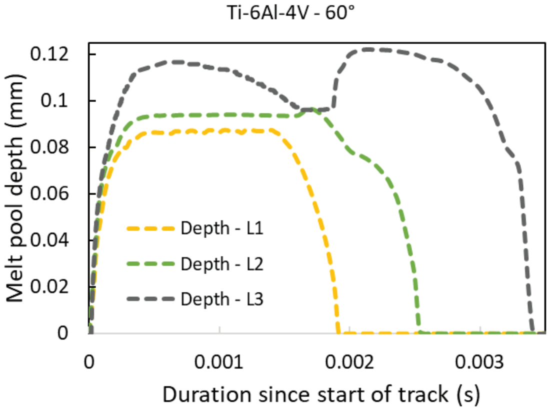 | 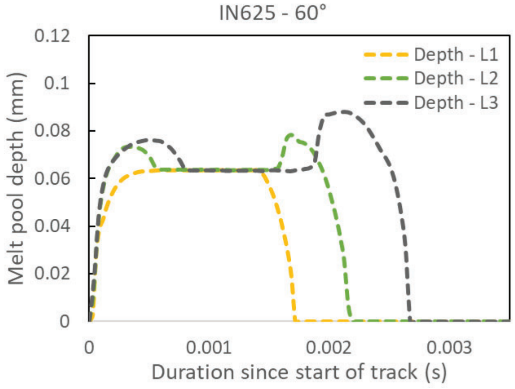 | 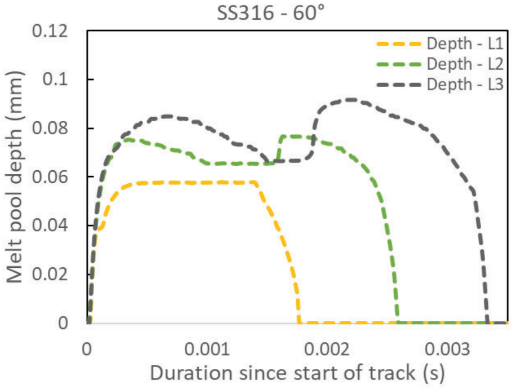 | 60 ° |

Table 4: Percentage increase in melt pool depth at the overhang region at 2nd and 3rd layers

| | **SS 316L** | | **IN625** | | **Ti-6Al-4V** | |
|---|---|---|---|---|---|---|
| **Angle** | **2nd Layer** | **3rd Layer** | **2nd Layer** | **3rd Layer** | **2nd Layer** | **3rd Layer** |
| 30 | 0.9% | 1.5% | 2.1% | 2.2% | 0.1% | 2.5% |
| 45 | 15.2% | 21.4% | 15.1% | 16.3% | 0.4% | 18.0% |
| 60 | 18.1% | 38.0% | 22.9% | 39.1% | 2.6% | 27.1% |

The simulation results for multiple materials demonstrate that the melt pool shape and geometry does not change much for overhang angles less than 30°. As observed, the melt pool depth increases with higher overhang angles. However, the exact trend in this melt pool dimension may vary with material. It has been shown that the subsequent overhangs allow reduced thermal dissipation due to low powder conductivity and store more energy thus producing deeper melt pools compared to the one formed in the initial overhang layer. More research is required to be able to predict the relation between material properties and the melt pool dimension.

## Conclusions

The heat transfer as a result of the L-PBF heat source interacting with the powder bed and solidified part consists of phase-change, melt pool dynamics and complex thermofluid phenomena – requiring the use of numerical simulation to understand process-property relationships for various metals. The effects of part orientation on this heat transfer can affect part quality – especially when parts have overhangs. The current work highlights the findings on the resulting melt pool that occurs as a result of negative draft angles. The following conclusions have been found for single-pass and multi-pass L-PBF of IN625, SS 316L and Ti-6Al-4V as laser powers 100 W and scan speeds of 500 mm/s:

1) The melt pool width does not depend heavily on overhang angle.
2) Maximum melt pool temperature slightly increases with higher overhang angle.
3) Melt pool depth is very sensitive to overhang angle. However, more work is needed to determine the number of subsequent layers in which the melt pool morphology stabilizes near the overhang region.
4) For overhang angles less than 30°, no variation in pool depth occurs.
5) Surface roughness characteristics and dimensional accuracy in the overhang region can be partially attributed to the unique thermal phenomena at the overhang region.

## Acknowledgements

This work has been supported by the National Institute of Standards and Technology (NIST) under contract No. 70NANB18H220. Some of this work was performed while Scott Thompson was a faculty member at Auburn University.

# References

[1] D. Rosenthal, The Theory of Moving Sources of Heat and Its Application to Metal Treatments, Trans. ASME. (1946) 849–866.

[2] A. Vasinonta, J.L. Beuth, M.L. Griffith, A Process Map for Consistent Build Conditions in the Solid Freeform Fabrication of Thin-Walled Structures, J. Manuf. Sci. Eng. 123 (2001) 615. doi:10.1115/1.1370497.

[3] A. Vasinonta, J.L. Beuth, M. Griffith, Process Maps for Predicting Residual Stress and Melt Pool Size in the Laser-Based Fabrication of Thin-Walled Structures, J. Manuf. Sci. Eng. 129 (2007) 101. doi:10/ft58cv.

[4] A.M. Rubenchik, W.E. King, S.S. Wu, Scaling laws for the additive manufacturing, J. Mater. Process. Technol. 257 (2018) 234–243. doi:10.1016/j.jmatprotec.2018.02.034.

[5] H. Peng, M. Ghasri-Khouzani, S. Gong, R. Attardo, P. Ostiguy, B.A. Gatrell, J. Budzinski, C. Tomonto, J. Neidig, M.R. Shankar, R. Billo, D.B. Go, D. Hoelzle, Fast prediction of thermal distortion in metal powder bed fusion additive manufacturing: Part 1, a thermal circuit network model, Addit. Manuf. 22 (2018) 852–868. doi:10/gf3jzm.

[6] M.P. Mughal, H. Fawad, R. Mufti, Finite element prediction of thermal stresses and deformations in layered manufacturing of metallic parts, Acta Mech. 183 (2006) 61–79. doi:10/dkwn4b.

[7] R. Andreotta, L. Ladani, W. Brindley, Finite element simulation of laser additive melting and solidification of Inconel 718 with experimentally tested thermal properties, Finite Elem. Anal. Des. 135 (2017) 36–43. doi:10.1016/j.finel.2017.07.002.

[8] T. Keller, G. Lindwall, S. Ghosh, L. Ma, B.M. Lane, F. Zhang, U.R. Kattner, E.A. Lass, J.C. Heigel, Y. Idell, M.E. Williams, A.J. Allen, J.E. Guyer, L.E. Levine, Application of Finite Element, Phase-field, and CALPHAD-based Methods to Additive Manufacturing of Ni-based Superalloys, Acta Mater. 139 (2017) 244–253. doi:10.1016/j.actamat.2017.05.003.

[9] V. Ankudinov, G.A. Gordeev, M.D. Krivilyov, Numerical simulation of heat transfer and melting of Fe-based powders in SLM processing, IOP Conf. Ser. Mater. Sci. Eng. 192 (2017) 012026. doi:10.1088/1757-899X/192/1/012026.

[10] W. Sudnik, D. Radaj, S. Breitschwerdt, W. Erofeew, Numerical simulation of weld pool geometry in laser beam welding, J. Phys. Appl. Phys. 33 (2000) 662–671. doi:10.1088/0022-3727/33/6/312.

[11] S.M. Thompson, L. Bian, N. Shamsaei, A. Yadollahi, An overview of Direct Laser Deposition for additive manufacturing; Part I: Transport phenomena, modeling and diagnostics, Addit. Manuf. 8 (2015) 36–62. doi:10/gd7gqw.

[12] W.J. Sames, F.A. List, S. Pannala, R.R. Dehoff, S.S. Babu, The metallurgy and processing science of metal additive manufacturing, Int. Mater. Rev. 61 (2016) 315–360. doi:10.1080/09506608.2015.1116649.

[13] M.J. Matthews, G. Guss, S.A. Khairallah, A.M. Rubenchik, P.J. Depond, W.E. King, Denudation of metal powder layers in laser powder bed fusion processes, Acta Mater. 114 (2016) 33–42. doi:10.1016/j.actamat.2016.05.017.

[14] S. Shrestha, S. Rauniyar, K. Chou, Thermo-Fluid Modeling of Selective Laser Melting: Single-Track Formation Incorporating Metallic Powder, J. Mater. Eng. Perform. 28 (2019) 611–619. doi:10/gf3jxw.

[15] N. Makoana, I. Yadroitsava, H. Möller, I. Yadroitsev, Characterization of 17-4PH Single Tracks Produced at Different Parametric Conditions towards Increased Productivity of LPBF Systems—The Effect of Laser Power and Spot Size Upscaling, Metals. 8 (2018) 475. doi:10/gfbm34.

[16] M. Masoomi, J.W. Pegues, S.M. Thompson, N. Shamsaei, A numerical and experimental investigation of convective heat transfer during laser-powder bed fusion, Addit. Manuf. 22 (2018) 729–745. doi:10/gf3jx4.

[17] P. Hartunian, M. Eshraghi, Effect of Build Orientation on the Microstructure and Mechanical Properties of Selective Laser-Melted Ti-6Al-4V Alloy, J. Manuf. Mater. Process. 2 (2018) 69. doi:10.3390/jmmp2040069.

[18] A. Ataee, Y. Li, D. Fraser, G. Song, C. Wen, Anisotropic Ti-6Al-4V gyroid scaffolds manufactured by electron beam melting (EBM) for bone implant applications, Mater. Des. 137 (2018) 345–354. doi:10/gctnxs.

[19] A. Yadollahi, N. Shamsaei, S.M. Thompson, A. Elwany, L. Bian, Effects of building orientation and heat treatment on fatigue behavior of selective laser melted 17-4 PH stainless steel, Int. J. Fatigue. 94 (2017) 218–235. doi:10.1016/j.ijfatigue.2016.03.014.

[20] M. Simonelli, Y.Y. Tse, C. Tuck, Effect of the build orientation on the mechanical properties and fracture modes of SLM Ti–6Al–4V, Mater. Sci. Eng. A. 616 (2014) 1–11. doi:10.1016/j.msea.2014.07.086.

[21] J.C. Fox, S.P. Moylan, B.M. Lane, Effect of Process Parameters on the Surface Roughness of Overhanging Structures in Laser Powder Bed Fusion Additive Manufacturing, Procedia CIRP. 45 (2016) 131–134. doi:10.1016/j.procir.2016.02.347.

[22] J.J. Valencia, P.N. Quested, Thermophysical Properties, (2008) 468–481. doi:10.1361/asmhba0005240.

[23] M. Boivineau, C. Cagran, D. Doytier, V. Eyraud, M.-H. Nadal, B. Wilthan, G. Pottlacher, Thermophysical Properties of Solid and Liquid Ti-6Al-4V (TA6V) Alloy, Int. J. Thermophys. 27 (2006) 507–529. doi:10/b2fwt2.

[24] C. Tang, J.L. Tan, C.H. Wong, A numerical investigation on the physical mechanisms of single track defects in selective laser melting, Int. J. Heat Mass Transf. 126 (2018) 957–968. doi:10/gf3jx6.

[25] S. Ghosh, L. Ma, L.E. Levine, R.E. Ricker, M.R. Stoudt, J.C. Heigel, J.E. Guyer, Single-Track Melt-Pool Measurements and Microstructures in Inconel 625, JOM. 70 (2018) 1011–1016. doi:10.1007/s11837-018-2771-x.

[26] S.S. Sih, J.W. Barlow, The Prediction of the Emissivity and Thermal Conductivity of Powder Beds, Part. Sci. Technol. 22 (2004) 427–440. doi:10.1080/02726350490501682.

[27] M.R. Alkahari, T. Furumoto, T. Ueda, A. Hosokawa, R. Tanaka, M.S. Abdul Aziz, Thermal Conductivity of Metal Powder and Consolidated Material Fabricated via Selective Laser Melting, Key Eng. Mater. 523–524 (2012) 244–249. doi:10/gf3jzg.

[28] L.C. Wei, L.E. Ehrlich, M.J. Powell-Palm, C. Montgomery, J. Beuth, J.A. Malen, Thermal conductivity of metal powders for powder bed additive manufacturing, Addit. Manuf. 21 (2018) 201–208. doi:10/gf3jzw.

[29] E.R. Denlinger, V. Jagdale, G.V. Srinivasan, T. El-Wardany, P. Michaleris, Thermal modeling of Inconel 718 processed with powder bed fusion and experimental validation using in situ measurements, Addit. Manuf. 11 (2016) 7–15. doi:10.1016/j.addma.2016.03.003.

[30] C.D. Boley, S.C. Mitchell, A.M. Rubenchik, S.S.Q. Wu, Metal powder absorptivity: modeling and experiment, Appl. Opt. 55 (2016) 6496. doi:10.1364/AO.55.006496.

## Appendix

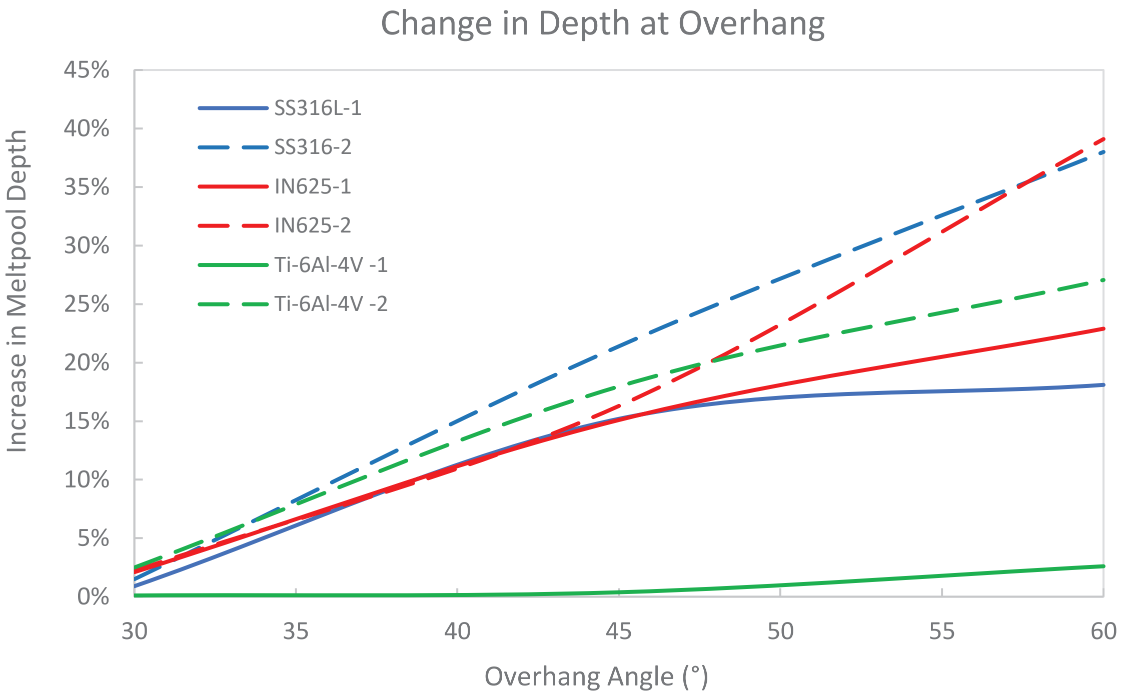A. Plot of change in melt pool depth for different overhang angles